The 2020 Mw6.0 Jiashi earthquake: Coinvolvement of thin-skinned thrusting and basement-shortening in shaping the Keping-tage nappe

Yuqing He[1], Teng Wang[1], Lihua Fang[2], Li Zhao[1]

[1]School of Earth and Space Sciences, Peking University, Beijing 100089, China.

[2]Institute of Geophysics, China Earthquake Administration, Beijing 100081, China.

Corresponding author: Teng Wang (wang.teng@pku.edu.cn)

Key Points:

- The shallow north-dipping low-angle thrust faulting dominated the rupture of the 2020 Mw6.0 Jiashi earthquake.
- A left-lateral tear fault and a south-dipping basement fault involved in the event.
- The surface deformation implies the basin-ward orogeny of the southwest Tian Shan.

Abstract

The Keping-tage fold-thrust belt in southwest Tian Shan is seismically active, yet most well-recorded earthquakes occurred south of the mountain front, hindering our understanding of the orogenic process to the north. The 2020 Mw6.0 Jiashi earthquake is an important event with surface deformation in the nappe structure well illuminated by InSAR. Here, we employ the surface deformation and relocated aftershocks to investigate the fault slip distribution associated to this event. Further added by an analysis of Coulomb stress changes, we derive a fault model involving slips on a shallow low-angle (~10^{o}) north-dipping thrust fault as well as on a left-lateral tear fault and a high-angle south-dipping reverse fault in mid crust. Our results reflect the basement-involved shorterning activated by a thin-skinned thrust faulting event with the surface deformation implying the basin-ward orogenic process of the southwest Tian Shan.

Plain Language Summary

Interferometric Synthetic Aperture Radar (InSAR) is an effective technique to image the surface deformation caused by earthquakes and can be a powerful tool for studying earthquake mechanism. Aftershock distribution can help delineate faults at depth and analyze regional earthquake risk. The 2020 Mw6.0 Jiashi earthquake raises concerns for seismic risk in the southwest Tian Shan seismic belt and provides a rare opportunity to illuminate the deformation and development of the southwest Tian Shan. Here, we combine InSAR deformation measurements and relocated aftershocks to investigate the faults responsible for this earthquake. Tests of different fault models show that the combination of a shallow thrust fault and two deeper faults can best explain the surface deformation and aftershock distribution. Stress analysis suggests that slips on the shallow fault reactivated the older basement structure at depth. Our results indicate that this earthquake uplifted the southmost mountain front with relatively low topography and therefore indicates the basin-ward propagation of the southwest Tian Shan.

1 Introduction

The Tian Shan region accommodates part of the ongoing Indo-Eurasian collision since ~20-25 Ma (Tapponnier et al., 1977; Avouac et al., 1993; Abdrakhmatov et al., 1996; Yang et al., 2008). As an intra-continental orogenic belt located 1000-2000 km north of the main Himalaya collision zone, the deformation is distributed along the broadly NE-SW trending Tian Shan (Yin et al., 1998; Allen et al., 1999). Along the southern Chinese Tian Shan, multiple fold-thrust fault zones were formed due to the late Paleozoic continent-continent collision with the Tarim Basin (Yin et al., 1998; Scharer et al., 2004), in which the westernmost Kashi-Akesu thrust segment hosts the Keping-tage fold-thrust belt (Figure 1a; Yin et al., 1998; Li et al., 2020). The Keping Fault has developed in the frontier of the belt, dipping generally to the north and are upwardly steep, forming a listric structure with ramp and flat segments soling into a main basal décollement at a depth of ~10 km (e.g., Scharer et al., 2004; Tian et al., 2006; Song et al., 2006; Gao et al., 2013; Zhang et al., 2019). Being in the triple junction of the Pamir syntaxis, the South Tian Shan and the Tarim Basin (Allen et al., 1999), earthquakes with diverse mechanisms occur intensively in the Keping-tage fold-thrust belt, especially in the past 20 years or so (Figure 1a, gray beachballs). However, most of the events are located south of the belt, and no large earthquake beneath the nappe structure has been studied with modern geodetic observations, hindering the understanding on the role of earthquakes in forming the arcuate emergent imbricate structures in this region.

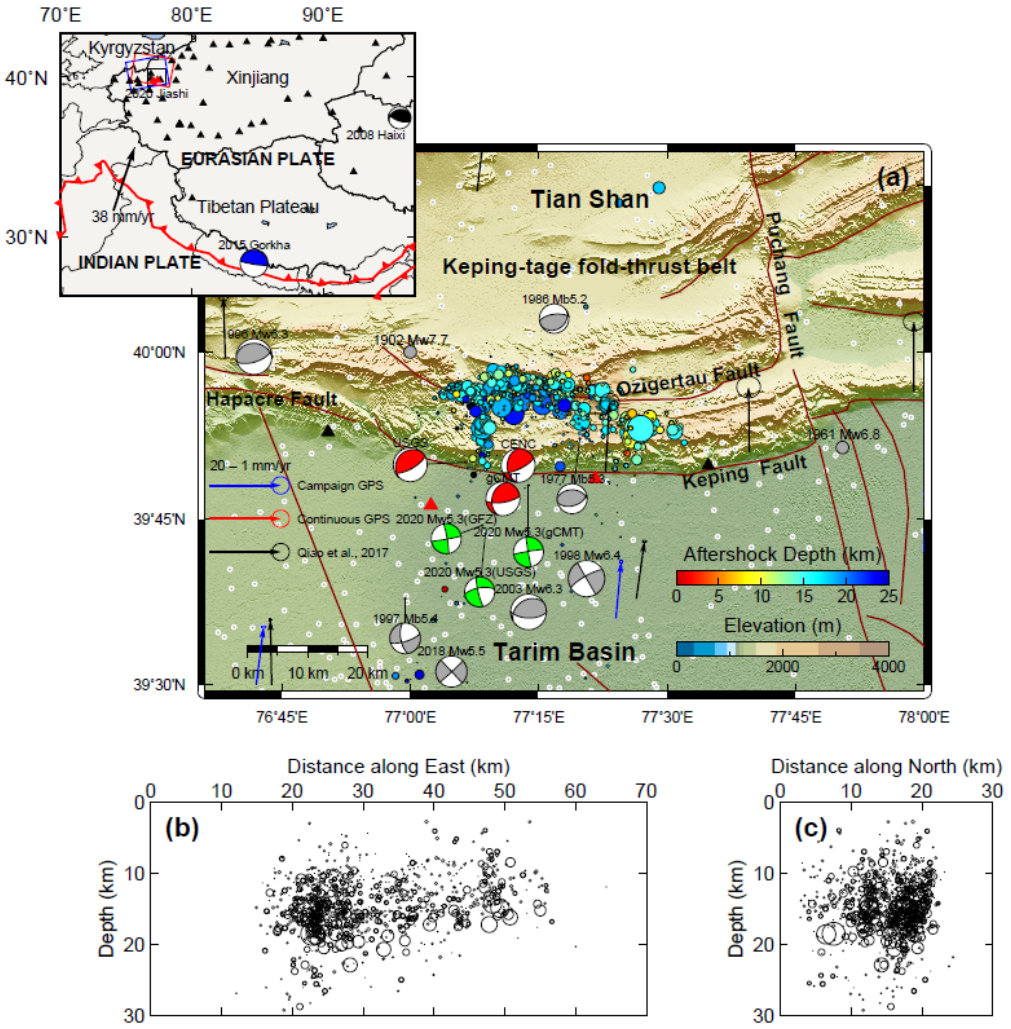

Figure 1. Tectonic settings and aftershock distribution of the January 19, 2020 Mw6.0 Jiashi earthquake. (a) Dark red lines depict active faults in this region. Arrows show the GPS horizontal velocities with respect to the Eurasian Plate (blue and red, Zhao et al., 2015; black, Qiao et al., 2017). Red beachballs display focal mechanisms of the Mw6.0 Jiashi earthquake from USGS, gCMT and CENC. Green beachballs depict focal mechanisms of the Mw5.3 event (2 days before the Mw6.0 event) from gCMT, USGS and GFZ. Gray dots denote background seismicity from the USGS catalog. Gray dots and beachballs show locations and/or focal mechanisms of recorded historical events in the Keping-tage zone, including the 1902 Mw7.7 Atushi earthquake (location only, Zhang et al., 1999; He et al., 2001), the 1961 Mw6.8 Bachu earthquake (location only), the 1977 Mb5.3 Xekar earthquake (Fan et al., 1994), the 1996 Mw6.3 Atushi earthquake, the 1986 Mb5.2 southern Xinjiang earthquake (Ekström and England, 1989), the Jiashi strong earthquake swarm in 1997-1998 (Zhou et al., 2001; Xu et al., 2005), the 2013 Mw6.3 Bachu-Jiashi earthquake (Wang et al., 2005), and the 2018 Mw5.5 Jiashi earthquake (Song et al., 2019). Black and red triangles represent permanent seismic stations and portable instruments deployed by the Xinjiang Earthquake Administration after the event. Aftershocks (up to February 22, 2020) are shown as circles color-coded by focal depths and size-scaled to

magnitudes. The topleft inset shows the location of the study area. Black triangles are seismic stations used in the aftershock relocation. Blue and red rectangles indicate the coverage of SAR data. Beachballs represent the two shallow-dipping thrust earthquakes discussed in this study. (b) and (c) show projections of all relocated aftershocks onto east-west and north-south vertical planes, respectively, with the size of circles proportional to the magnitude.

On January 19, 2020, an Mw6.0 earthquake occurred in the Keping fold-thrust belt, striking Jiashi County in southern Xinjiang, China. The United States Geological Survey (USGS), global CMT (gCMT) and China Earthquake Networks Center (CENC) all located the event at the south edge of the thrust zone, and reported predominately thrust slips occurring on either a low-angle plane dipping north or a high-angle plane dipping south, both trending in the EW direction (Figure 1a; Table S1). Preliminary slip inversions using InSAR observations prefer the shallow north-dipping plane with mainly thrust slips and slight strike-slip components (Yu et al., 2020; Yao et al., 2020). However, the discrepancies between the InSAR and seismology derived dip angles and focal depths are quite large (Table S1). Focal mechanisms from gCMT and USGS W-phase inversion show a large non-double-couple component (both are ~27%), indicating a complex rupture process. Interestingly, on January 17, 2020, an Mw5.3 strike-slip earthquake occurred ~12 km south of the Mw6.0 event, probably ruptured a NS-trending sub-vertical fault plane with a left-lateral slip (Figure 1a, green beachballs). These early studies suggest that the fault geometry and rupture process of the 2020 Jiashi earthquake may be more complex than those revealed by individual type of data.

Because of the moderate size of the Jiashi event, teleseismic records may have sparse coverage and limited signal-to-noise ratios to resolve the rupture process (e.g., Institute of Tibetan Plateau Research, Chinese Academy of Sciences, http://www.itpcas.ac.cn/kycg/yjcg/202001/t20200122_5494135.html). InSAR observations can provide high-resolution, near-field constraints to quantify the fault geometry and spatial slip distribution, yet it may lack the ability to resolve the fault configuration at depth. After the earthquake, the Xinjiang Earthquake Administration deployed 2 portable seismic instruments (red triangles in Figure 1a) to augment the

seismic network. Together with the 11 existing seismic stations within 150 km of the epicenter (Figure 1), ~1900 aftershocks were recorded by February 21, 2020, with significantly greater depths than the InSAR derived fault plane (Yu et al., 2020; Yao et al., 2020), suggesting the possible reactivation of basement faults.

Here, we combine InSAR observations and relocated aftershocks to image the seismogenic structure of the 2020 Mw6.0 Jiashi event. We first obtain the surface deformation from Sentinel-1 interferograms to determine the fault geometry and slip distribution on the main rupture area. We then search for the optimal combination of faults with different dipping angles and depths by fitting both the surface deformation and aftershock distribution. Combining the InSAR and seismology results with an analysis of Coulomb stress changes, we propose a conceptual fault model involving a shallow north-dipping thrust fault, a strike-slip tear fault and a south-dipping high-angle basement fault to explain the paradox between InSAR derived fault plane and aftershock distribution. Our results reveal the complexity of this event and shed lights on its role in the orogeny of southwest Tian Shan.

2 Methods

2.1 Aftershock relocation

The ~1900 aftershocks recorded by the regional seismic network from January 19 to February 21, 2020 were relocated using the double-difference algorithm (Waldhauser and Ellsworth, 2000) with the 1-D P-wave velocity model from the CRUST1.0 model (Laske et al., 2013). After the relocation procedure, we obtained locations of 1506 aftershocks with magnitudes of $-1.6 \leq M \leq 5.2$. We used 976 aftershocks with $M \geq 0$ to illuminate the fault geometry at depth (Figure 1).

2.2 InSAR data processing

We collected Sentinel-1 SAR images spanning the earthquake from ascending (AT129) and descending (DT34) tracks (Table S2). The interferograms were obtained using the Sentinel-1 Interferometry Processor (Jiang et al., 2017) and unwrapped by SNAPHU software (Chen and Zebker, 2001). The unwrapped interferograms were

149 down sampled using the quadtree method (Jonsson, 2002), resulting in 614 and 498
150 data points for ascending and descending tracks, respectively (Figure S1).

151 2.3 Inversion of fault geometry and slip distribution

152 We adopted a two-step procedure to obtain the optimal fault geometry and slip
153 distribution (e.g., Jonsson, 2002). The InSAR measurements were used to estimate the
154 optimal fault parameters using the Geodetic Bayesian Inversion Software (GBIS;
155 Bagnardi and Hooper, 2018). Then, we extended the fault plane in the dip and strike
156 directions to invert for the corresponding slip distributions using the steepest descent
157 method (Wang et al., 2009). In order to evaluate the data fitness, a dimensionless
158 misfit is calculated using the weighted residual sum of squares (WRSS), considering
159 the data covariance matrix (Xue et al., 2010).

160 2.4 Coulomb failure stress change

161 To investigate the potential relationship between the shallow north-dipping fault
162 and aftershocks as well as the seismic risk on the adjacent faults, we calculated the
163 change of Coulomb failure stress (ΔCFS) utilizing the Coulomb 3.3 software (Toda et
164 al., 2011) with an effective friction coefficient of 0.4 and a shear modulus of 30 GPa.
165 In using our fault models, we ignored the segments with slips less than 0.1 m and
166 calculated ΔCFS on the derived fault planes, the high-angle segment of the Keping
167 Fault and the Puchang Fault east of the epicenter.

168 3 Results

169 3.1 Aftershock distribution

170 The relocated aftershocks exhibit two distinct clusters in a generally T-shaped zone
171 (Figure 1a). One is mainly distributed along the Ozigertau fold with a nearly EW
172 extension of ~40 km, the other is geometrically conjugate to the first one and
173 concentrated in a narrow zone, extending ~20 km northward from the Keping Fault to
174 the Ozigertau Fault (Figure 1a). The depths of these aftershocks are mainly 10-25 km
175 in the mid crust (Figures 1b and 1c). According to previous studies, the depth of the

176 detachment fault below the Keping Fault is ~10 km (e.g., Scharer et al., 2004). The
177 aftershocks thus likely occurred on structures beneath the detachment fault.

178 The first cluster can be fitted by an EW-striking, south-dipping plane with a high
179 dip angle of 84°; whereas aftershocks in the western cluster can be fitted by a
180 sub-vertical NS-striking fault plane, similar to one of the nodal planes of the Mw5.3
181 earthquake that occurred two days before the Mw6.0 event (Figure 1a, green
182 beachballs). From their spacial distribution, the two fault planes may intersect at depth.
183 Note that aftershocks and after-slips occurred on these two fault planes may also
184 contribute to InSAR measurements, as the SAR images were acquired 9 (ascending)
185 and 3 (descending) days after the main event.

186 ### 3.2 InSAR derived deformation field

187 The interferograms (Figures 2a and 2b) exhibit a clear deformation pattern that
188 shows two elliptical areas elongated in the EW direction with clear fringes spreading
189 ~50 km. The deformation patterns from ascending and descending orbits are similar,
190 suggesting that the line-of-sight (LOS) displacements mainly reflect the vertical
191 motion. The earthquake caused ~5 cm of subsidence on the northern Ozigertau fold
192 lobe, and ~7 cm of uplift between the EW-striking Keping and Ozigertau faults,
193 implying that this event mainly ruptured a gently-dipping fault between these two
194 faults (Figures 2c and 2d). The subsidence area coincides with the EW-trending
195 aftershock cluster. No phase discontinuity is observed from both interferograms,
196 indicating that the rupture did not reach the surface. Deformation and topography
197 profiles along the NS direction display an obvious ‘bell-shaped’ pattern. Uplift
198 occurred in the area of relatively low elevation, while subsidence occurred in the area
199 of relatively high elevation (Figures 2e and 2f).

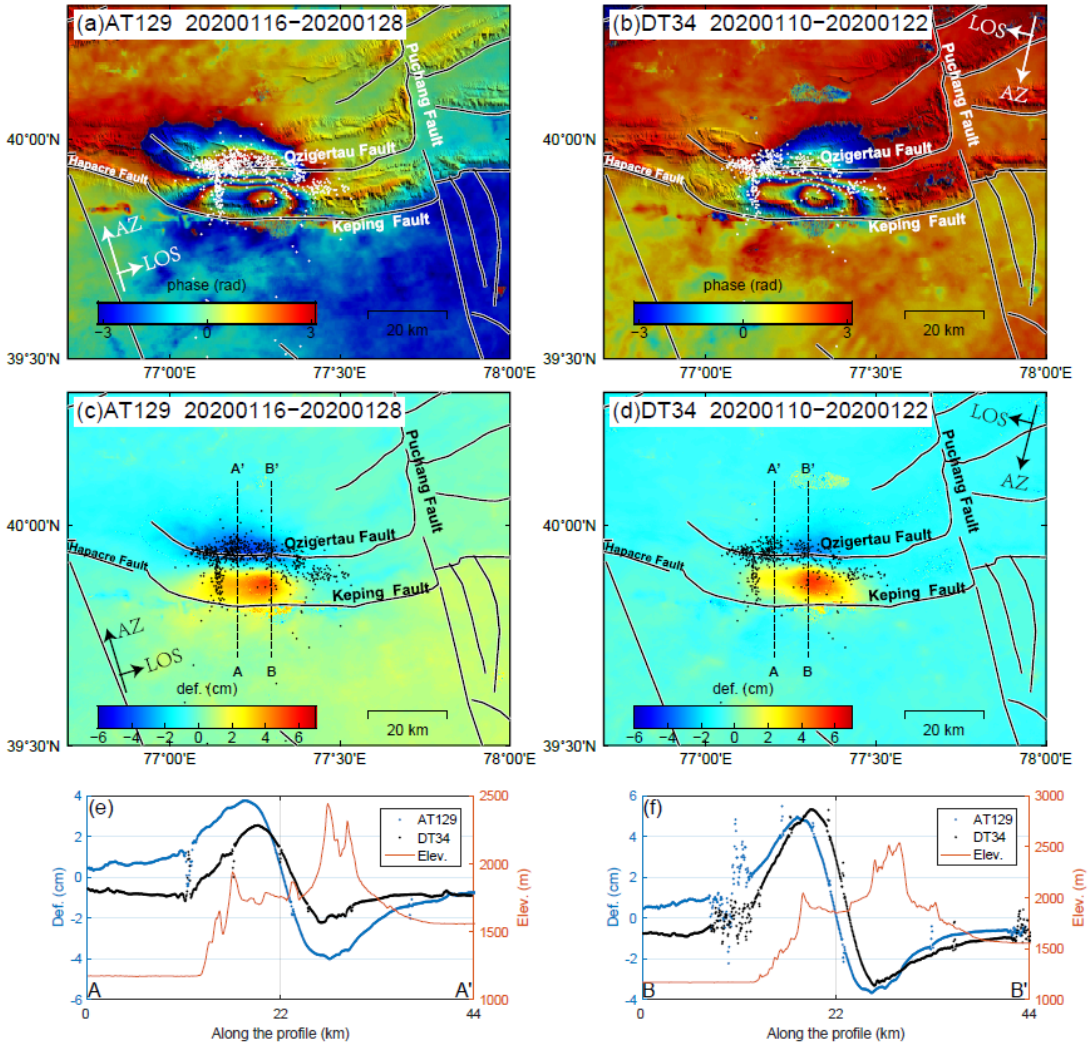

Figure 2. Surface deformation associated with the 2020 Mw6.0 Jiashi earthquake from Sentinel-1 SAR interferograms. (a) and (b) show interferograms from ascending (AT129) and descending (DT34) tracks, respectively. Each fringe represents 2.8 cm of line-of-sight deformation. White dots show relocated aftershocks during the SAR acquisition time. (c) and (d) show the corresponding deformation with black dots representing aftershock distributions. (e) and (f) display the deformations (DT34 in blue and AT129 in black) along the NS profiles AA' and BB', respectively, with the elevation shown in orange.

3.3 Single fault geometry and slip distribution

Due to the fault plane ambiguity in focal mechanisms, reverse slips on either a high-angle, south-dipping fault or on a low-angle north-dipping fault can cause similar surface deformation patterns for the main event. We therefore set both nodal planes as initial fault in our geodetic inversion (Models 1 and 2 in Table S3). Results show that the surface deformation can be better fitted by a 10.2° ± 7.4° north-dipping fault with a depth of 6.9 ± 1 km (Model 1). The detailed inversion results and data

fitness are provided in Figures S2-S9 and Tables S3-S5. Our preferred model has a smaller dip angle (10.2º) than the 20º in the model presented in Yao et al. (2020), but is generally consistent with the 9º from the USGS body-wave mechanism and the 8.8º in Yu et al. (2020) (Table S1).

The slip distribution in our preferred model displays predominantly thrust motion with a slight left-lateral strike-slip component (Figures 3 and S6). The slips are mainly distributed in a depth range of ~6-8.5 km, and probably arrested by the detachment fault at ~10 km depth. Assuming a Poisson's ratio of 0.25 and a shear modulus of 30 GPa, the geodetic moment is $\sim 1.332 \times 10^{18}$ N·m, i.e., Mw6.08, which is slightly larger than that obtained from USGS and gCMT (Mw6.0).

3.4 Coulomb stress change

To analyze the possible triggering effect between the shallow north-dipping fault and deep aftershocks, we calculated the Coulomb stress changes caused by our preferred single-fault model to the deep south-dipping and strike-slip faults inferred from aftershock distribution. Due to the lack of focal mechanisms of aftershocks, we set strike-slip (left- and right-lateral) mechanisms on sub-vertical NS-trending faults, as well as strike-slip, reverse and normal mechanisms on faults dipping 84° to the south as receiving faults (Figures 4d-4l and S10). Results show that aftershocks of the western cluster mainly fall in the area with increased Coulomb stress when a left-lateral strike-slip fault is used as the receiving fault (zone ‘A’, Figures 4d-4f). The nearly EW-distributed aftershocks are well located in the loading area of the Coulomb stress when the south-dipping fault is set as a reverse fault (zone ‘B’, Figures 4g-4i). The Coulomb stress changes exceed the triggering threshold of 0.1 bar (Kilb et al., 2000), implying that the shallow north-dipping fault may have a large triggering effect on the complex deep structures. Interestingly, a few aftershocks at depth of ~15 km to the east are well located in the loading area for a right-lateral strike-slip fault plane (zone ‘C’, Figures 4j-4l).

The Coulomb stress changes due to the Mw6.0 event on the adjacent mapped faults

244 are relatively small. Even though the loading effect on the shallow high-angle
245 segment of the Keping Fault has reached the loading threshold at ~4 km, few
246 aftershocks occurred shallower than 5 km (Figure S11). The rupture of the low-angle
247 thrust has a certain triggering effect on subsequent seismic activity outside the rupture
248 area at depths of 5-9 km (Figure S12). The Coulomb stress on the middle segment of
249 the strike-slip Puchang Fault (Figure 1a) has slightly increased at the shallow depth of
250 0-10 km (~0.05 bar; Figure S13).

251 ### 3.5 Multi-fault geometry and slip distribution

252 Although our shallow north-dipping model can explain the InSAR observations
253 reasonably well, the large none-double-couple component revealed from the
254 seismological data and the deep aftershock distribution imply that multiple faults may
255 be involved during the 2020 Jiashi event. We therefore designed another 4 models
256 with multi-fault configurations (Models 3-6 in Table S3), where fault geometries of
257 the two deep faults are inferred from relocated aftershocks with faulting mechanisms
258 from analysis of Coulomb stress changes (Table S6). When we added the deep
259 south-dipping and strike-slip faults delineated by aftershocks to the shallow
260 north-dipping fault model, the data-model correlation increases from 96.92% to
261 97.93%, and the misfit decreased from 0.0274 to 0.0226 (Table S3, Figures 3c-3h and
262 Figures S14-S19). The deep faults alone yield a very poor data fitness with a
263 data-model correlation of 79.59% (Model 5 in Table S3 and Figure S19), strongly
264 suggesting that aftershocks and main slips were distributed on different fault planes.
265 The rupture on all three faults yields a moment magnitude of Mw6.17, which is larger
266 than the magnitude obtained by seismic data (Mw6.0). Considering that aftershocks
267 and after slips may cause surface deformation as well, part of the observed surface
268 signal maybe caused by these post-seismic processes.

269 Although our InSAR observations do not have enough temporal resolution to
270 distinguish coseismic and early post-seismic deformation, given the relatively large
271 left-lateral strike-slip component in the gCMT, we propose that the NS-trending fault

may have ruptured coseismically, consistent with the early Mw5.3 strike-slip event. We obtain a new moment tensor by superimposing the shallow north-dipping and the deep strike-slip faults, which is more consistent with solutions from gCMT and USGS W-phase than the one derived from a single north-dipping thrust obtained by InSAR data (Figure 3b). The seismologically determined epicenter of the Mw6.0 event is located near the southern tip of the NS-trending fault defined by relocated aftershocks, rather than the location of maximum thrust slip. Thus, the Mw6.0 event might be initiated on the strike-slip fault and then propagated to the north. We do not have sufficient evidence to conclude whether the deep south-dipping fault ruptured coseismically. Further studies on joint inversion may yield more detailed image of the dynamic rupture process.

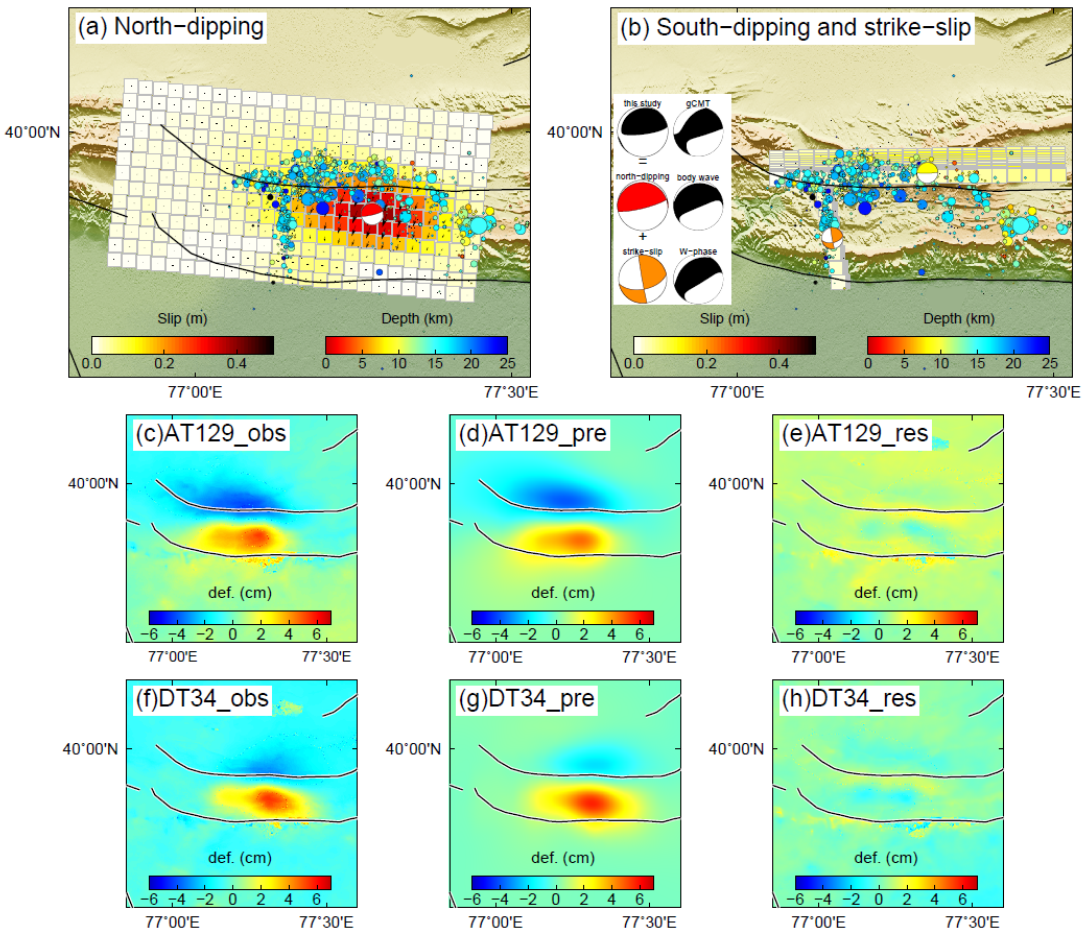

Figure 3. Map views of the slip distributions on (a) the shallow north-dipping fault and (b) the deep south-dipping and strike-slip faults inferred from aftershock distribution. Red, orange, and yellow beachballs depict the focal mechanism of the north-dipping thrust fault, the deep strike-slip fault and the south-dipping reverse fault, respectively. Circles represent relocated aftershocks as in Figure 1. (c-h) Observed,

289 predicted and the residual maps based on our preferred Model 6 in Table S3 for the
290 ascending (top row) and the descending tracks (bottom row).

291 4 Discussion and conclusions

292 4.1 Coinvolvement of shallow thrusting and basement-shortening during the 2020
293 Jiashi earthquake

294 Moderate-sized earthquakes can have complex ruptures and complicated aftershock
295 distributions, which have been illuminated by surface ruptures (e.g., Lo et al., 2019)
296 and/or regional and near-field seismological observations (e.g., Poli et al., 2016). In
297 contrast, the 2020 Jiashi earthquake exhibits a rather simple and smooth surface
298 deformation, making it difficult to resolve the faulting complexity using InSAR data
299 alone. Yu et al. (2020) propose that the area below the main rupture is
300 stress-enhancing. Our Coulomb stress analysis is consistent with their conclusion yet
301 with more details, thanks to the relocated aftershocks (Figures 4d-4l).

302 Our modeling reveals a high-angle south-dipping structure located well beneath the
303 detachment fault. Plenty of basement faults have been identified in the Tarim Basin,
304 cutting through both the basement or the sedimentary covers, and mainly located at
305 the margin of the basin, where both normal and thrust faults have developed (Lin et
306 al., 2015). The marginal basement faults are mainly thrust faults with basin-ward
307 inclination, and their directions are consistent with the basin's boundaries. As the Tian
308 Shan overthrust the Tarim Basin since ~20-25 Ma (e.g., Tapponnier et al., 1977;
309 Avouac et al., 1993; Li et al., 2020), the detected deep south-dipping reverse fault
310 may be an old structure belonging to the Tarim block. Triggered by the shallow slips
311 during the 2020 Jiashi earthquake, the basement fault might be reactivated, leading to
312 aftershocks. The inferred south-dipping basement fault also suggests the development
313 of basement shortening during a shallow, thin-skinned thrust event with moderate size
314 (e.g., Lacombe and Mouthereau, 2002).

315 Different shortening rates have been observed among different segments of the
316 Keping-tage nappe throughout the Cenozoic period (Li et al., 2020). Therefore, along

its southern margin, the nearly NS-trending strike-slip faults play important roles in regulating the along-strike variation of collision rates, e.g., the Puchang Fault (Figure 1a; Yin et al., 1998; He et al., 2002; Zhang et al., 2019; Li et al., 2020). Several strike-slip earthquakes occurred south of the Keping-tage fold-thrust zone (Figure 1a). Similar to these strike-slip faults, the blind left-lateral strike-slip fault delineated by the 2020 Mw5.3 earthquake and the nearly NS-trending aftershocks may also be the consequence of different shortening rates. Aftershocks to the east of the main rupture area might also indicate a right-lateral strike-slip blind fault (Figures 4a-4b and 4j-4l). Together with the left-lateral fault to the west, they exhibit a block of box-like extrusion bounded by two tear faults (Figures 4a and 4b). We infer that the strike-slip tear faults at depth may extend to the south of the fold-thrust zone, adjusting the variation of shortening rates in this region.

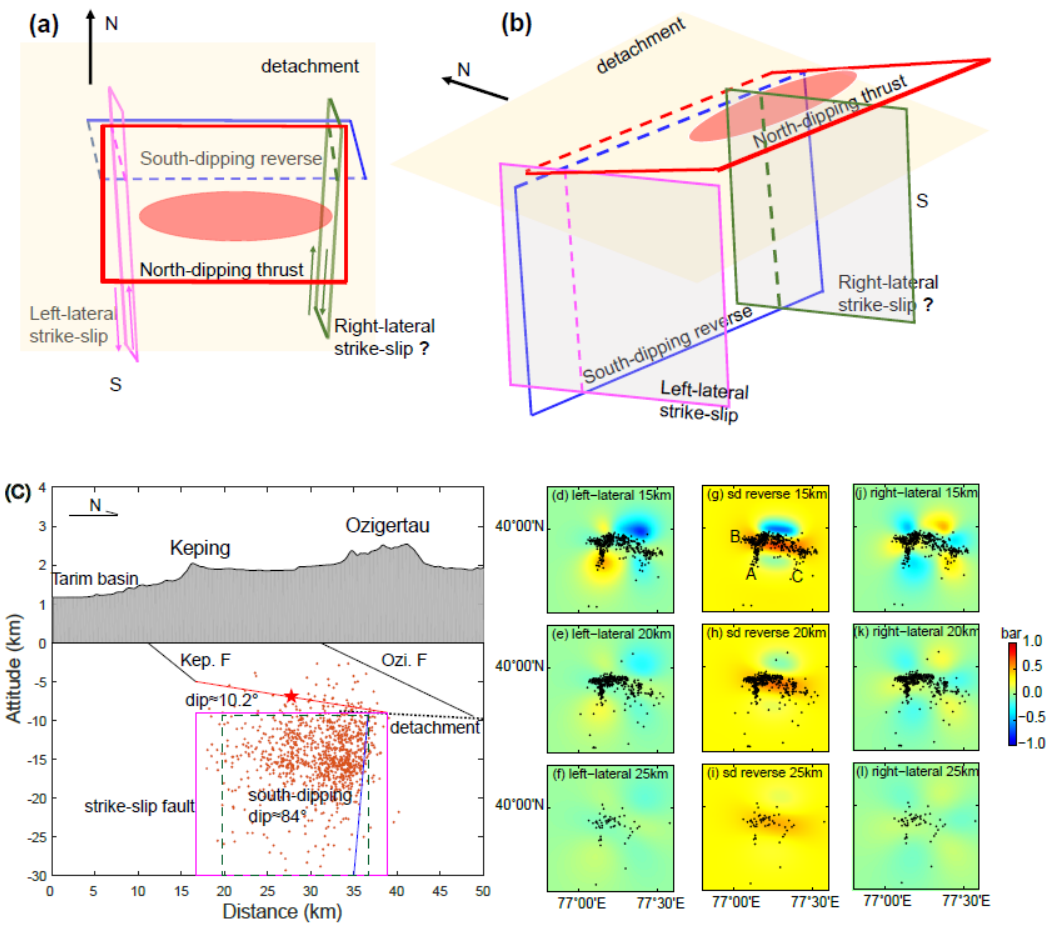

Figure 4. Seismogenic faults during the 2020 Jiashi earthquake. (a) and (b) shows top and side views of the conceptual model. (c) NS projection of faults and all relocated aftershocks. Red star represents the centroid of the slip distribution on the shallow

north-dipping Keping thrust segment (red box). The magenta and dark green boxes are side views of the deep left-lateral and right-lateral strike-slip faults, respectively, and the blue line represents the deep south-dipping reverse fault delineated by aftershocks. Kep.F: Keping Fault; Ozi.F: Ozigertau Fault. (d-l) Changes of Coulomb stress at depths of 15 km, 20 km and 25 km due to the rupture of shallow north-dipping thrust on the deep left-lateral fault to the west (d-f), the deep south-dipping reverse fault beneath the main rupture area (g-i), and the deep right-lateral fault to the east (j-l). Black dots show epicenters of aftershocks at corresponding depths. A, B and C represent the three main aftershocks distribution zones.

Note that due to the sparse near-field seismic stations and the large topographical fluctuations in this region, aftershock relocation based on simple 1-D velocity model may have larger uncertainty in hypocentral depth. Focal mechanisms of aftershocks and detailed geological investigations are required to further interpret structures beneath the detachment fault.

4.2 Basin-ward orogenic process revealed by the surface deformation

The 2020 Mw6.0 Jiashi event is the first earthquake occurred beneath the Keping fold-thrust belt to be well imaged by geodetic data, providing a rare opportunity to study the role of earthquakes in shaping the topography in a nappe tectonic setting. This event lowered the high mountain along the Ozigertau Fault, whereas uplifted the relatively lower mountain front along the youngest Keping thrust, likely implying propagation of the orogenic deformation into the basin. This type of surface deformation has also been observed in other intracontinental low-angle thrust events, such as the 2008 Mw6.3 Haixi, Qinghai earthquake (Daout et al., 2019) and the 2015 Mw7.8 Gorkha, Nepal earthquake (Elliott et al., 2016) (Table S6 and beachballs in Figure 1 inset). Due to the flattern effect of this event, we suspect that the long-term aseismic process or plastic folding contribute positively to the local topography in this region.

We conclude that the January 2020 Mw6.0 Jiashi earthquake involves ruptures of a multi-fault system in both shallow and mid crust. The deformation pattern reveals the basin-ward propagation of orogenic deformation in shaping the nappe structure during

the low-angle thrust faulting. Further analyses are necessary to apply InSAR observations to resolve the deformation in the post- and inter-seismic stages and quantify the contributions of elastic and plastic deformation during the orogenic process in southwest Tian Shan.

Acknowledgments

Figures are generated by the Generic Mapping Tools 5.4.3 (Wessel et al., 2013). Sentinel-1 SAR imges are copyrighted by the European Space Agency and processed by the Sentinel-1 Interferometry Processor software (Jiang et al., 2017) (available at http://sarimggeodesy.github.io/software). We are grateful for insightful discussions with Heng Luo from Wuhan University and Xuhua Shi from Zhejiang University. This work has been supported by the National Science Foundation of China (Grants 42021003, U1939202, 41974017 and 41774067). The data and model in this study can be accessed at https://disk.pku.edu.cn:443/link/E1479A04ADBC76C0A1C077C37B061B2C

References

Allen, M. B., Vincent, S. J., & Wheeler, P. J. (1999). Late cenozoic tectonics of the Kepingtage thrust zone: Interactions of the Tien Shan and Tarim Basin, northwest China. *Tectonics*, 18(4), 639-654.

Avouac, J. P., Tapponnier, P., Bai, M., You, H., & Wang, G. (1993). Active Thrusting and Folding Along the Northern Tien-Shan and Late Cenozoic Rotation of the Tarim Relative to Dzungaria and Kazakhstan. *Journal of Geophysical Research-Solid Earth*, 98(B4), 6755-6804.

Abdrakhmatov, K. Y., Aldazhanov, S. A., Hager, B. H., Hamburger, M. W., Herring, T. A., Kalabaev, K. B., et al. (1996). Relatively recent construction of the Tien Shan inferred from GPS measurements of present-day crustal deformation rates. *Nature*, 384(6608), 450-453.

Bagnardi, M., & Hooper, A. (2018). Inversion of Surface Deformation Data for Rapid Estimates of Source Parameters and Uncertainties: A Bayesian Approach. *Geochemistry Geophysics Geosystems*, 19(7), 2194-2211.

Chen, C. W., & Zebker, H. A. (2001). Two-dimensional phase unwrapping with use of statistical models for cost functions in nonlinear optimization. *Journal of the Optical Society of America a-Optics Image Science and Vision*, 18(2), 338-351.

Daout, S., Sudhaus, H., Kausch, T., Steinberg, A., & Dini, B. (2019). Interseismic and Postseismic Shallow Creep of the North Qaidam Thrust Faults Detected with a Multitemporal InSAR Analysis. *Journal of Geophysical Research-Solid Earth*,

124(7), 7259-7279.

Elliott, J. R., Jolivet, R., Gonzalez, P. J., Avouac, J. P., Hollingsworth, J., Searle, M. P., & Stevens, V. L. (2016). Himalayan megathrust geometry and relation to topography revealed by the Gorkha earthquake. *Nature Geoscience*, 9(2), 174-180.

Ekström, G., & England, P. (1989). Seismic Strain Rates in Regions of Distributed Continental Deformation. *Journal of Geophysical Research-Solid Earth and Planets*, 94(B8), 10231-10257.

Fan, G. W., Ni, J. F., & Wallace, T. C. (1994). Active Tectonics of the Pamirs and Karakoram. *Journal of Geophysical Research-Solid Earth*, 99(B4), 7131-7160.

Gao, R., Hou, H. S., Cai, X. Y., Knapp, J. H., He, R. Z., Liu, J. K., et al. (2013). Fine crustal structure beneath the junction of the southwest Tian Shan and Tarim Basin, NW China. *Lithosphere*, 5(4), 382-392.

He, W. Y., Li, J. H., Qian, X. L., & Zheng, D. M. (2002). Analysis of fault structures in the Kalpin fault uplift, Tarim Basin. *Geology In China*, 29 (001): 37-43. (in Chinese).

He, Y. M., Zheng, T. Y., & Shan, X. J. (2001). March 19, 1996 Artux Xinjiang Earthquake: A Simple Unilateral Rupture Event. *Chinese Journal of Geophysics*, 44(4), 510-519. (in Chinese).

Jiang, H. J., Feng, G. C., Wang, T., & Burgmann, R. (2017). Toward full exploitation of coherent and incoherent information in Sentinel-1 TOPS data for retrieving surface displacement: Application to the 2016 Kumamoto (Japan) earthquake. *Geophysical Research Letters*, 44(4), 1758-1767.

Jonsson, S., Zebker, H., Segall, P., & Amelung, F. (2002). Fault slip distribution of the 1999 M-w 7.1 Hector Mine, California, earthquake, estimated from satellite radar and GPS measurements. *Bulletin of the Seismological Society of America*, 92(4), 1377-1389.

Kilb, D., Gomberg, J., & Bodin, P. (2000). Triggering of earthquake aftershocks by dynamic stresses. *Nature*, 408(6812), 570-574.

Lacombe, O., & Mouthereau, F. (2002). Basement-involved shortening and deep detachment tectonics in forelands of orogens: Insights from recent collision belts (Taiwan, Western Alps, Pyrenees). *Tectonics*, 21(4), 12-1-12-22.

Lo, Y. C., Yue, H., Sun, J. B., Zhao, L., & Li, M. J. (2019). The 2018 M(w)6.4 Hualien earthquake: Dynamic slip partitioning reveals the spatial transition from mountain building to subduction. *Earth and Planetary Science Letters*, 524, art. no. 115729. https://doi.org/10.1016/j.epsl.2019.115729

Laske, G., Masters., G., Ma, Z. and Pasyanos, M. (2013). Update on CRUST1.0 - A 1-degree Global Model of Earth's Crust, *Geophys. Res. Abstracts*, 15, Abstract EGU2013-2658.

Lin, B., Zhang, X., Xu, X. C., Yuan, J. Y., Neng, Y., & Zhu, J. W. (2015). Features and effects of basement faults on deposition in the Tarim Basin. *Earth-Science Reviews*, 145, 43-55.

Li, A., Ran, Y. K., Gomez, F., Jobe, J. A. T., Liu, H. G., & Xu, L. X. (2020). Segmentation of the Kepingtage thrust fault based on paleoearthquake ruptures,

444 southwestern Tianshan, China. *Natural Hazards*, 103(1), 1385-1406.
445 Poli, P., Prieto, G. A., Yu, C. Q., Florez, M., Agurto-Detzel, H., Mikesell, T. D., et al.
446 (2016). Complex rupture of the M6.3 2015 March 10 Bucaramanga earthquake:
447 evidence of strong weakening process. *Geophysical Journal International*, 205(2),
448 988-994.
449 Qiao, X. J., Yu, P. F., Nie, Z. S., Li, J., Wang, X. Q., Kuzikov, S. I., et al. (2017). The
450 Crustal Deformation Revealed by GPS and InSAR in the Northwest Corner of the
451 Tarim Basin, Northwestern China. *Pure and Applied Geophysics*, 174(3),
452 1405-1423.
453 Scharer, K. M., Burbank, D. W., Chen, J., Weldon, R. J., Rubin, C., Zhao, R., & Shen,
454 J. (2004). Detachment folding in the Southwestern Tian Shan-Tarim foreland,
455 China: shortening estimates and rates. *Journal of Structural Geology*, 26(11),
456 2119-2137.
457 Song, F. M., Min, W., Han, Z. J., & Xu, X. W. (2006). Cenozoic deformation and
458 propagation of the Kalpintag fold nappe. *Seismology And Geology*, 28 (002):
459 224-233. (in Chinese).
460 Song, C. Y., Gao, R., Liu, J. M., Liu, P., Guo, Y., & Wen, S. Y. (2019). Discussion on
461 earthquake sequence and seismogenic structure for the Jiashi Ms5.5 earthquake
462 on September 4, 2018, Xinjiang. *Earthquake Research China*, 35(2), 256-268. (in
463 Chinese).
464 Toda, Shinji, Stein, R.S., Sevilgen, Volkan, & Lin, Jian, 2011, Coulomb 3.3
465 Graphic-rich deformation and stress-change software for earthquake, tectonic,
466 and volcano research and teaching—user guide: U.S. Geological Survey
467 Open-File Report 2011–1060, 63 p., available at
468 https://pubs.usgs.gov/of/2011/1060/
469 Tian, Q. J., Ding, G. Y., & Hao, P. (2006). Seismotectonic study on west part of the
470 interaction zone between southern TianShan and northern Tarim. *Seismology And*
471 *Geology*, 28(002), 213-223. (in Chinese).
472 Tapponnier, P., & Molnar, P. (1977). Active Faulting and Tectonics in China. *Journal*
473 *of Geophysical Research*, 82(20), 2905-2930.
474 Wessel, P., Smith, W. H. F., Scharroo, R., Luis, J., & Wobbe, F. (2013). Generic
475 mapping tools: Improved version released. Eos, *Transactions of the American*
476 *Geophysical Union*, 94(45), 409-410. https://doi.org/10.1002/2013eo450001.
477 Waldhauser, F., & Ellsworth, W. L. (2000). A double-difference earthquake location
478 algorithm: Method and application to the northern Hayward fault, California.
479 *Bulletin of the Seismological Society of America*, 90(6), 1353-1368.
480 Wang, W. M., Li, L., Zhao, L. F., Li, J., & Yao, Z. X. (2005). Rupture process of Jiashi,
481 Xinjiang earthquake (Ms6.5) of Feb. 24, 2003. *Chinese Journal of Geophysics*,
482 48 (2), 343-351. (in Chinese).
483 Wang, L., Wang, R., Roth, F., Enescu, B., Hainzl, S., & Ergintav, S. (2009). Afterslip
484 and viscoelastic relaxation following the 1999 M 7.4 Izmit earthquake from GPS
485 measurements. *Geophysical Journal International*, 178(3), 1220-1237.
486 Xu, Y., Steven, W. R., Wei, R. P., Zhang, W. L., & Wei, B. (2005). Analysis of seismic
487 activity in the crust from earthquake relocation in the Central Tian Shan. *Chinese*

Journal Of Geophysics, 48(6), 1308-1315. (in Chinese).

Xue, L., Sun, J. B., & Shen, Z. K. (2011). InSAR coseismic deformation observation of the Jan 12 th, 2010 Haiti earthquake and its coseismic slip distribution inversion. *Seismology And Geology*, 033(001):157-174. (in Chinese).

Yang, X. P., Deng, Q. D., Zhang, P. Z., Xu, X. W. (2008). Crustal shortening of major nappe structures on the front margins of the Tianshan. *Seismology And Geology*, 30(1), 111-131. (in Chinese).

Yu, P., Qiao, X., Xiong, W. et al. (2020). Source model for the Mw 6.0 earthquake in Jiashi, China on 19 January 2020 from Sentinel-1A InSAR data. *Earth Planets Space*, 72, 169. https://doi.org/10.1186/s40623-020-01300-4

Yin, A., Nie, S., Craig, P., Harrison, T. M., Ryerson, F. J., Qian, X. L., & Yang, G. (1998). Late Cenozoic tectonic evolution of the southern Chinese Tian Shan. *Tectonics*, 17(1), 1-27.

Zhou, S. Y., Xu, Z. H., Chen, X. F. (2001). Analysis on the source characteristics of the 1997 Jiashi swarm, western China. *Chinese Journal Of Geophysics*, (05), 75-83. (in Chinese).

Zhao, B., Huang, Y., Zhang, C. H., Wang, W., Tan, K., & Du, R. L. (2015). Crustal deformation on the Chinese mainland during 1998-2014 based on GPS data. *Geodesy and Geodynamics*, 6(1), 7-15.

Zhang, G. M., Zhu, L. R., Song, X. D., Li, Z. X., Yang, M. L., Su, N. Q., & Chen, X. Z. (1999). Predictions of the 1997 strong earthquakes in Jiashi, Xinjiang, China. *Bulletin of the Seismological Society of America*, 89(5), 1171-1183.

Zhang, Y., S. Yang, H. Chen, Y. Dilek, X. Cheng, X. Lin, C. Wang, and T. Zhu (2019), The effect of overburden thickness on deformation mechanisms in the Keping fold-thrust belt, southwestern Chinese Tian Shan Mountains: Insights from analogue modeling, Tectonophysics, 753, 79-92.